Available online at www.sciencedirect.com

SCIENCE DIRECT®

International Journal of Heat and Fluid Flow 24 (2003) 480–490

International Journal of
HEAT AND
FLUID FLOW

www.elsevier.com/locate/ijhff

Drag reduction in turbulent pipe flow with feedback control applied partially to wall

Koji Fukagata [a,b,*], Nobuhide Kasagi [a]

[a] Department of Mechanical Engineering, The University of Tokyo, 7-3-1 Hongo, Bunkyo-ku, Tokyo 113-8656, Japan
[b] Institute for Energy Utilization, AIST, 1-2-1 Namiki, Tsukuba-shi, Ibaraki 305-8564, Japan

Received 23 November 2002; accepted 5 March 2003

Abstract

Turbulent pipe flow controlled by the opposition control algorithm [J. Fluid Mech. 262 (1994) 75–110] is studied by means of direct numerical simulation. A special focus is laid upon a scheme in which the control input is applied only partially over a limited length in the streamwise direction, but not on the entire wall surface. The upstream control effect remains over a distance of about 11–14 times the pipe radius downstream of the point where the control is terminated. This results, however, in a simple relationship that the average drag reduction rate is nearly proportional to the control length. The recovery process after the control termination is quantitatively investigated by applying a recently proposed exact relation between the skin friction and the Reynolds stress distribution [Phys. Fluids 14 (11) (2002) L73–L76] and also by performing a budget analysis specially designed for that purpose.

Keywords: Pipe flow; Turbulence; Control; Drag reduction; Direct numerical simulation; Opposition control; Partial control; Reynolds stress budget

1. Introduction

During the last decade, so-called active feedback control of turbulent flow has attracted much attention. Its application is diverse, e.g., reduction of skin friction drag of aircrafts and carrier ships, enhancement of mixing in heat exchangers and bioreactors, and noise reduction of high-speed vehicles.

An active feedback control system generally consists of three functional hardware components, i.e., sensors, controllers and actuators, and an additional software component, i.e., a control algorithm which determines the action of actuators depending upon the sensor output. In parallel with intensive R&D studies of hardware components, the control algorithm has been developed and assessed by using direct numerical simulation (DNS) of controlled turbulent flow fields.

Choi et al. (1994) attained considerable drag reduction in their DNS of turbulent channel flow by local wall blowing and suction, of which velocity is determined so as to oppose the velocity components induced by the near-wall quasi-streamwise vortices. Their study assumed a highly idealized situation: use of a virtual detection plane in the flow, blowing and suction actuators continuously distributed over a wall surface, and flows at low Reynolds numbers. Later efforts were devoted to develop alternative control algorithms so that similar control effects can be attained in more realistic control system. Lee et al. (1998), by using the suboptimal control approach and the knowledge obtained by the opposition control, proposed a simple algorithm that uses information on the wall surface instead of a virtual detection plane. Discrete wall-deformation actuators were assumed by Endo et al. (2000) instead of spatially continuous blowing and suction. More recently, the control effects at higher Reynolds numbers were investigated (Iwamoto et al., 2002; Chang et al., 2002). These studies demonstrated that the strategy essentially similar to the opposition control proposed by Choi et al. (1994) should be, with a slight deterioration, effective even for the drag reduction in more practical situations.

Most of the previous studies dealt with plane channel flows. A flow in a circular pipe is another canonical wall-bounded flow and its control has several direct practical

---

* Corresponding author. Address: Department of Mechanical Engineering, The University of Tokyo, 7-3-1 Hongo, Bunkyo-ku, Tokyo 113-8656, Japan. Tel.: +81-3-5841-6419; fax: +81-3-5800-6999.
E-mail address: fukagata@thtlab.t.u-tokyo.ac.jp (K. Fukagata).

0142-727X/03/$ - see front matter © 2003 Elsevier Science Inc. All rights reserved.
doi:10.1016/S0142-727X(03)00058-4

applications. Very recently, Xu et al. (2002) derived the analytical suboptimal solution for drag reduction in a turbulent pipe flow, which results in a quite similar form to that in a channel flow (Lee et al., 1998). They report that the control effects are also similar. However, this is the only work reported on the active feedback control applied to pipe flows and therefore the control algorithms proposed for channel flows should further be tested in pipe flows.

More importantly, the previous studies always assumed control inputs applied on the entire wall surface. In reality, it may not be possible both technologically and financially to have an entire wall surface equipped with an array of active feedback control units. In many perspective cases, the number of sensors and actuators should be limited. Currently, several attempts are ongoing in order to prove the active feedback/feedforward drag reduction control in laboratory experiments (Rathnasingham and Breuer, submitted for publication; Yoshino et al., 2002). In the experiment by Rathnasingham and Breuer (submitted for publication), local drag reduction is attained by using a few sets of sensors/actuators. However, at the moment, one cannot evaluate how many sets of sensors/actuators or how large area of control may be required in order to truly prove the net drag reduction effect because the knowledge on spatially inhomogeneous control is lacking.

The objective of the present study is, therefore, to investigate by means of DNS the effects of the opposition control (Choi et al., 1994), where the control is applied only on a limited wall surface area of a cylindrical pipe. Variation of the skin friction coefficient along the streamwise direction is quantitatively analyzed.

2. Numerical method

The governing equations are the incompressible continuity and the Navier–Stokes equations expressed in the cylindrical coordinates. The DNS code used in the present study is based on a second-order accurate finite difference scheme on the cylindrical coordinate system. The computational grids are stretched in the radial (r) direction and equally spaced in the azimuthal (θ) and longitudinal (z) directions. A special care is taken on the consistency in the discretized space, so that the energy is conserved in the computation of the inviscid part of the governing equation as well as in the treatment of the singular pole (Fukagata and Kasagi, 2002). The time integration is advanced by using the low storage third-order accurate Runge–Kutta scheme (Spalart et al., 1991) for the advection terms and the Crank–Nicolson scheme for the diffusion terms. The same coefficients as those used by Rai and Moin (1991) are used. For the pressure coupling, a delta-form fractional step method is used. The Poisson equation is solved using trigonometric expansions. The statistics of an uncontrolled flow computed by using the present code are in excellent agreement with previous DNS data. Further details of the computational method used and the validation of the present DNS code are documented in Fukagata and Kasagi (2002).

Throughout the present study, the mass flow rate is kept constant. Several test cases are set at a relatively low bulk Reynolds number, $Re_\mathrm{b} = 2U_\mathrm{b}R/\nu = 5300$, which corresponds to the friction Reynolds number of $Re_{\tau\mathrm{u}} = u_{\tau\mathrm{u}}R/\nu \simeq 180$ in the uncontrolled flow. Hereafter, super- and subscripts of ‘u’ are used for the dimensionless quantities normalized by the friction velocity of the uncontrolled flow, $u_{\tau\mathrm{u}}$, and the kinematic viscosity, ν. A fully developed turbulent flow is assumed in a circular pipe of a radius R, but the computation is made in a pipe of finite length L with periodic boundary conditions at both ends. Thus, strictly speaking, the flow field should be always periodic in the streamwise direction, and it is particularly so in the case with control applied partially to wall. The size of computational domain and computational mesh used are shown in Table 1.

The control algorithm used in the present study is the opposition control (v-control) proposed by Choi et al. (1994). Namely, the time-dependent, local blowing/suction velocity at the wall, $u_r(R, \theta, z, t)$, is given by

$$u_r(R, \theta, z, t) = -u_r(R - y_\mathrm{d}, \theta, z, t). \tag{1}$$

Here, y_d denotes the distance between wall and a virtual detection plane as shown in Fig. 1.

3. Fully applied control

In this section, the drag reduction performance is presented for the case where the opposition control applied on the entire wall.

Table 1
Computational conditions

Test case	$Re_{\tau\mathrm{u}}$	L_z/R	$L_z^{+\mathrm{u}}$	N_r	N_θ	N_z	$\Delta r^{+\mathrm{u}}$	$(R\Delta\theta)^{+\mathrm{u}}$	$\Delta z^{+\mathrm{u}}$
Case 1	180	20	3600	96	128	512	0.46–2.99	8.84	7.03
Case 2	184	20	3680	48	128	256	0.95–6.11	9.03	14.4
Case 3	184	40	7360	48	128	512	0.95–6.11	9.03	14.4
Case 4	184	80	14720	48	128	1024	0.95–6.11	9.03	14.4

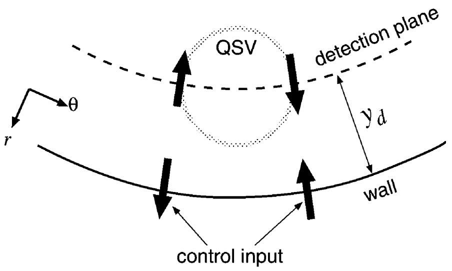

Fig. 1. Schematic of the active cancellation control in pipe.

Each simulation is started from a fully developed flow without control. The skin friction coefficient, $C_f = 2\tau_w/(\rho U_b^2)$, behaves similarly to that of a channel flow (Choi et al., 1994). In each case, the flow seems to reach a quasi-steady state after 500–1000 viscous time units. All the statistics shown below are obtained from the data accumulated over approximately 2000 time units after the flow is judged to be in a quasi-steady state.

Fig. 2 summarizes the relationship between y_d^{+u} and the drag reduction rate, $R_D = (C_{fu} - C_f)/C_{fu}$, where C_{fu} is the skin friction coefficient of the uncontrolled flow. Corresponding data for channel flow by Choi et al. ($y_d^{+u} \simeq 10$) and Hammond et al. (1998) ($y_d^{+u} \simeq 15$) for $Re_{\tau u} \simeq 180$ are also plotted. The dependency of R_D on y_d^{+u}, as well as the maximum drag reduction ($R_D \simeq 25\%$ at $y_d^{+u} \simeq 15$), is similar to that in the channel flow.

As can be judged from clear agreement between Cases 2 and 3, the length of the periodic computational domain is sufficiently long. The comparison between Cases 1 and 2 indicates that the drag reduction rates computed by using the finer and coarser grids have only little difference. Therefore, the coarser grid (Cases 2–4) is used throughout the following investigation.

Statistics of velocity and pressure are also accumulated, although not shown here. Modulation of these statistics due to control is similar to that in the channel flow. Interested readers are referred to the DNS database available at http://www.thtlab.t.u-tokyo.ac.jp/.

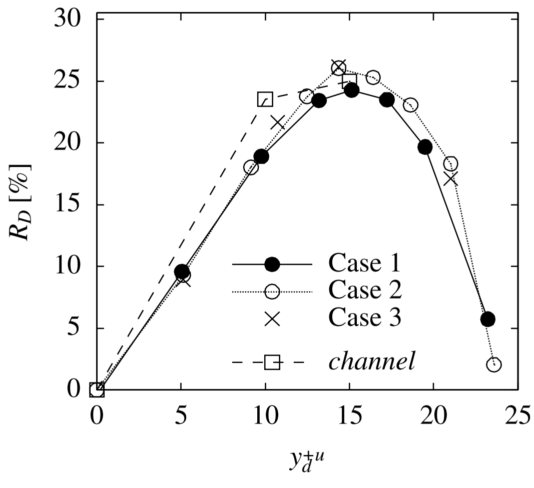

Fig. 2. Drag reduction rate, R_D, as functions of the detection plane height, y_d^{+u}.

4. Partially applied control

4.1. Average and local drag reduction rates

The control input is applied only in the region of $0 < z < L_c$ as shown in Fig. 3. Three different periodic lengths, which are identical to the computational domain lengths (Cases 2–4), are examined.

Fig. 4 shows the average drag reduction rate, R_D, as a function of L_c^{+u}. The drag reduction rate is nearly proportional to the ratio of control length to period, i.e., $R_D(\eta)/R_D(1) \simeq \eta$, where $\eta = L_c/L$. This relation is nearly independent of the choice of the period (see, the results of $y_d^{+u} = 10$ for $L^{+u} = 3680$ and $L^{+u} = 7360$). It is also found to be independent of the detection plane height ($y_d^{+u} = 10$, 15 and 20) as seen in the cases of $\eta = 0.5$.

Although the relationship between η and R_D is seemingly simple, the process under study is complex. This is illustrated by the streamwise variation of the

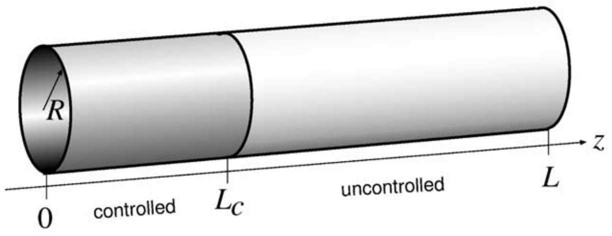

Fig. 3. Schematic of control applied partially to wall.

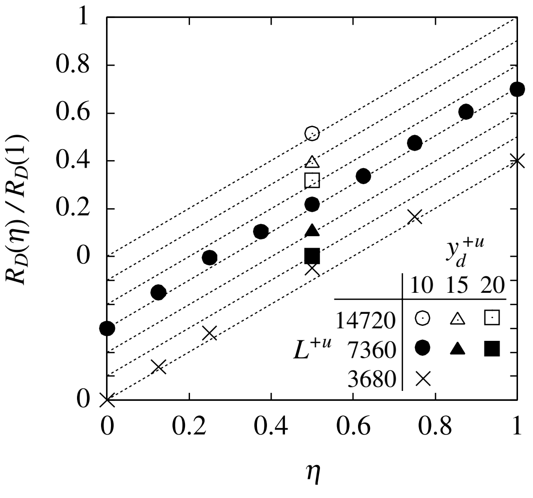

Fig. 4. Normalized average drag reduction rate, $R_D(\eta)/R_D(1)$, as a function of the ratio of control length to period, $\eta = L_c/L$.

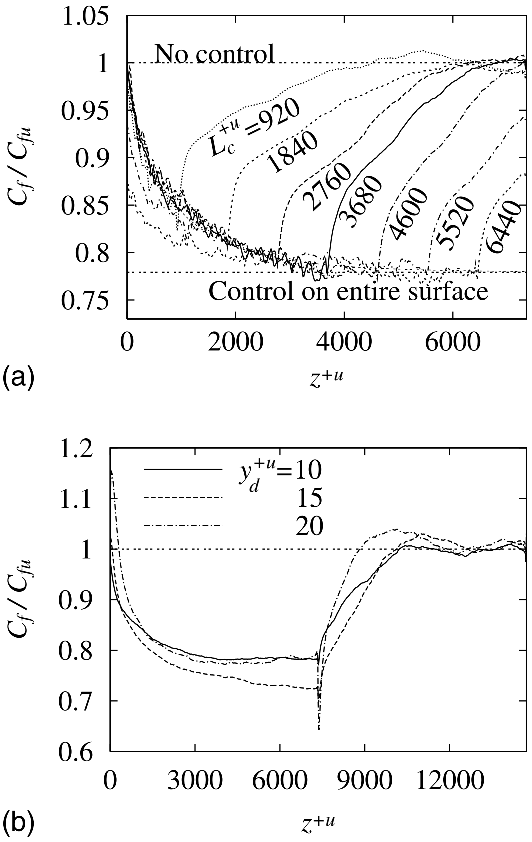

Fig. 5. Normalized local skin friction coefficient: (a) different control length (Case 3, $y_\mathrm{d}^{+\mathrm{u}} = 10$); (b) different detection plane height (Case 4, $L_\mathrm{c}^{+\mathrm{u}} = 7360$).

local skin friction coefficient, $C_\mathrm{f}(z)$, as shown in Fig. 5a. The common behavior observed regardless of the value of L_c is as follows. In the controlled region, C_f decreases following the single curve that can be curve-fitted as

$$C_\mathrm{f}(z^{+\mathrm{u}}) = C_\mathrm{fe} + (C_\mathrm{fu} - C_\mathrm{fe})\exp[-(z^{+\mathrm{u}}/a)^b], \tag{2}$$

where C_fe denotes the skin friction coefficient in the case of fully applied control, and a and b are constants. A least square fit gives $a \simeq 750$ and $b \simeq 0.76$. Just after the control ends, C_f rapidly increases. Subsequently, C_f increases almost linearly up to C_fu. The persistence length of control effect downstream of the controlled region is estimated as 2000–2500 wall units. As will be discussed later, the secondary gradual increase is dominated by the large scale on the order of the pipe radius. Therefore, the recovery length is scaled as $11R$–$14R$. This length is comparable to that after the reattachment downstream of a low-height backward facing step (Le et al., 1997). It is also worth noting that C_f does not recover to C_fu in the cases of $L_\mathrm{c}^{+\mathrm{u}} > 4600$ due to insufficient length for recovery, so that it follows a curve different from Eq. (2) in the beginning of the controlled region.

Similar behavior can be observed in the cases where a different detection plane height is adopted, as shown in Fig. 5b. The degree of complexity, however, increases as the detection plane is shifted higher. In the case of $y_\mathrm{d}^{+\mathrm{u}} \simeq 20$, for instance, C_f rapidly increases at the onset of control, and then reduces similarly to the case of $y_\mathrm{d}^{+\mathrm{u}} \simeq 10$. Around the control terminal edge, C_f impulsively drops before the rapid recovery. Apparently, the above-modeled curve, i.e., Eq. (2), is not universal and depends on $y_\mathrm{d}^{+\mathrm{u}}$. It may also be dependent on the control algorithm used. Nevertheless, the approximate shape of the curve may be useful for designing an experimental setup of the drag reduction system with any control algorithms that give similar effects as the opposition control.

In the present simulations, the boundary condition is suddenly changed at the interfaces of the controlled and uncontrolled regions. Therefore, one may be concerned with that the observations above and below may contain fictious (i.e., numerically generated) effects. In order to investigate on the magnitude of such numerical effects, we performed an additional simulation for Case 4 ($L_\mathrm{c}^{+\mathrm{u}} = 7360$, $y_\mathrm{d}^{+\mathrm{u}} = 15$) with a second-order explicit low-pass filter, i.e., $\phi_{jk}^{(\mathrm{filtered})} = (\phi_{jk-1} + 2\phi_{jk} + \phi_{jk+1})/4$, applied to the control input around the interfaces. Here, j and k denote the grid indices in the azimuthal and longitudinal directions, respectively. As shown in Fig. 6, the computational results with this filtered control input have only little difference from those with the unfiltered one. Thus, the observations presented here can be regarded as mostly physical.

Among the turbulence statistics calculated, the streamwise variation of the mean velocity and root-mean-square (rms) velocity and pressure fluctuations in Case 3 with $y_\mathrm{d}^{+\mathrm{u}} = 15$ and $L_z^{+\mathrm{u}} = 3680$ are shown in Fig. 7. The different lines represent the profiles at different streamwise positions. Here, $y^{+\mathrm{u}} = (R - r)^{+\mathrm{u}}$ is the distance from the wall in the wall unit of the uncontrolled flow. In the controlled region, the mean velocity is first distorted near the wall, and then the change gradually propagates towards the pipe axis. In the uncontrolled regions, on the other hand, it seems to recover

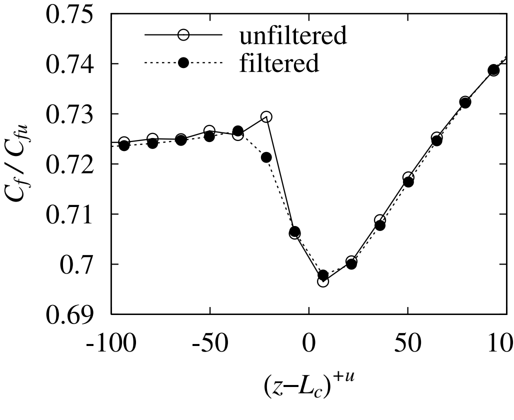

Fig. 6. Effects of the low-pass filter on the local skin friction coefficient (Case 4, $L_\mathrm{c}^{+\mathrm{u}} = 7360$, $y_\mathrm{d}^{+\mathrm{u}} = 15$).

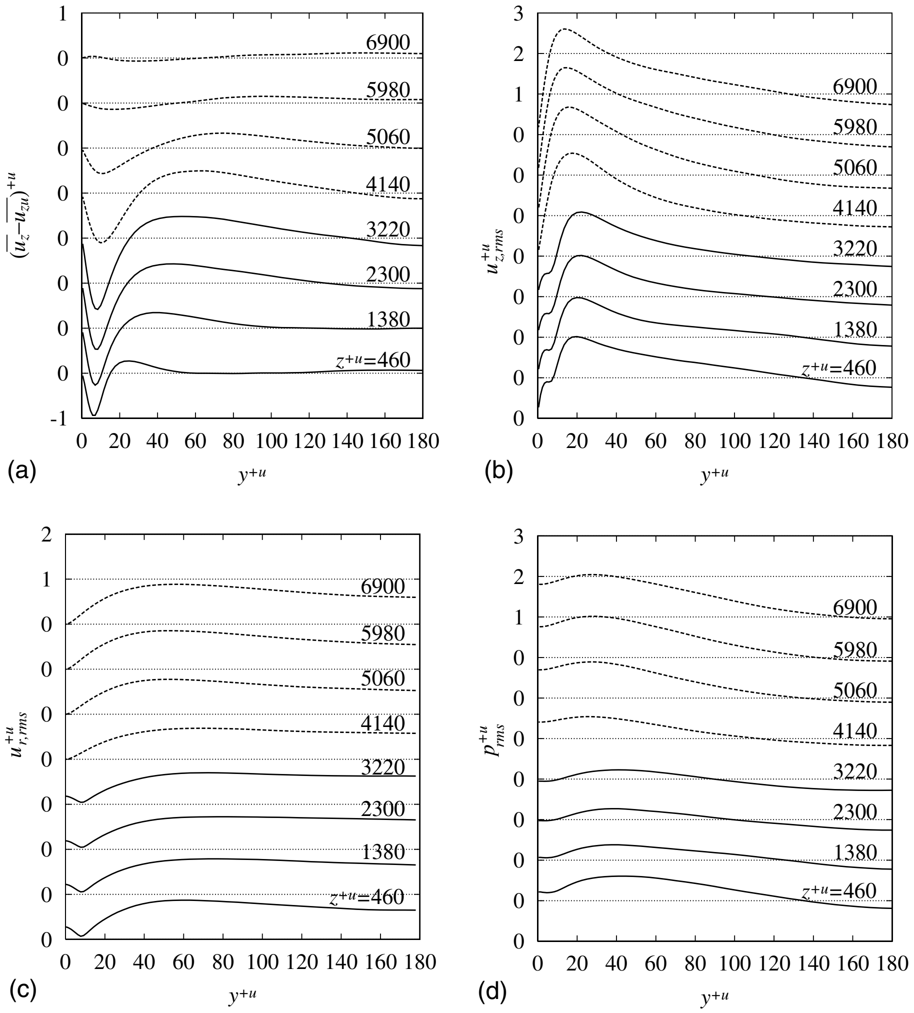

Fig. 7. Flow statistics (Case 3 with $L_z^+ = 3680$ and $y_d^{+u} = 15$): (a) deviation of mean velocity from uncontrolled flow; (b) rms longitudinal velocity fluctuation; (c) rms radial velocity fluctuation; (d) rms pressure fluctuation. Solid lines—controlled region; dashed lines—uncontrolled region.

uniformly. Variation in the profiles of rms velocity and pressure fluctuations seems to be more rapid. The shapes of these profiles are essentially the same within the controlled region and within the uncontrolled region, whereas they drastically change at the transition from the controlled to the uncontrolled region and vice versa. The location of the virtual wall, where $u_{r,\mathrm{rms}}$ becomes nearly zero (Hammond et al., 1998), is $y^{+\mathrm{u}} \simeq 9$ and almost unchanged throughout the controlled region.

4.2. Contributions to the streamwise variation of C_f

As illustrated above, the average drag reduction rate is simply proportional to the control length ratio, η, despite the complex flow evolution process in the streamwise direction. In real applications, it is desirable to keep the drag reduction effect sustaining even far downstream of the controlled region, so that a higher average drag reduction rate can be attained. This may be achieved by properly modifying the control input. In this subsection, detailed phenomena and the causes for the complex curve of C_f are discussed in order to obtain a clue for such modification of control input. Hereafter, all variables without superscript are those nondimensionalized by the pipe radius and twice the bulk mean velocity.

For the present flow condition, the skin friction coefficient is decomposed into the laminar contribution (C_f^L) that is identical to the well-known laminar solution, the turbulent contribution (C_f^T), and the inhomogeneous contribution (C_f^I) (Fukagata et al., 2002), i.e.,

$$C_\mathrm{f}(z) = \underbrace{\frac{16}{Re_\mathrm{b}}}_{C_\mathrm{f}^\mathrm{L}} + \underbrace{16\int_0^1 2r\overline{u'_r u'_z}\, r\,\mathrm{d}r}_{C_\mathrm{f}^\mathrm{T}} + \underbrace{16\int_0^1 (1-r^2)\left(I''_z + \frac{\partial p''}{\partial z}\right) r\,\mathrm{d}r}_{C_\mathrm{f}^\mathrm{I}}. \qquad (3)$$

Here, $\overline{(\cdot)}$ and $(\cdot)'$ denote the average and fluctuation based on the averaging in the homogeneous directions, respectively, i.e.,

$$f(r,\theta,z,t)=\bar{f}(r,z)+f'(r,\theta,z,t), \tag{4}$$

whereas the double prime $(\cdot)''$ represents deviation of the average $\overline{(\cdot)}$ from the local bulk mean quantity, i.e.,

$$\overset{\approx}{f}(z,t)=\int_0^1 2\bar{f}(r,z,t)r\,\mathrm{d}r, \tag{5}$$

and

$$f''(r,z,t)=\bar{f}(r,z,t)-\overset{\approx}{f}(z,t). \tag{6}$$

The third term of the right-hand side of Eq. (3) contains a statistical quantity related to $\overline{I_z}$ which represents the terms appearing in the Reynolds averaged Navier–Stokes equation when the flow is inhomogeneous in the streamwise direction, i,e.,

$$\overline{I_z}=\frac{1}{r}\frac{\partial(r\overline{u_r u_z})}{\partial r}+\frac{\partial(\overline{u_z u_z})}{\partial z}-\frac{1}{Re_\mathrm{b}}\frac{\partial^2\overline{u_z}}{\partial z^2}. \tag{7}$$

Fig. 8 shows the magnitudes of these contributions in Case 4 with $L_\mathrm{c}^{+\mathrm{u}}=7360$. The laminar contribution ($C_\mathrm{f}^\mathrm{L}\simeq 0.003$) and the turbulent contribution (C_f^T) are dominant, and the inhomogeneous contribution (C_f^I) is small in most of the region. The streamwise variation of C_f observed in Fig. 5a is essentially due to the variation of C_f^T, and the additional complexity in the cases with larger $y_\mathrm{d}^{+\mathrm{u}}$ (Fig. 5b) is attributed to that of C_f^I. Therefore, the cause for the complex variation of C_f can be studied by examining the distribution of the integrant in C_f^T, i.e., the weighted Reynolds shear stress.

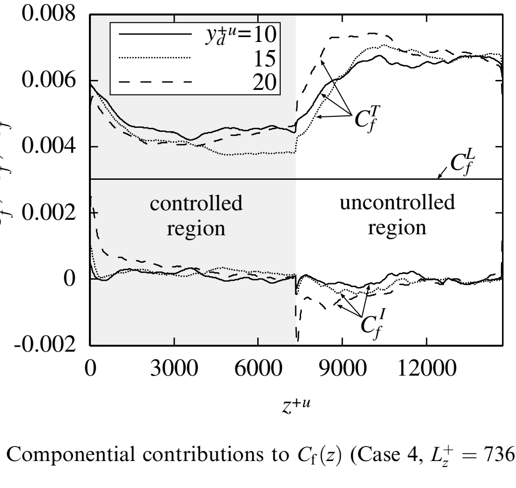

Fig. 8. Componential contributions to $C_\mathrm{f}(z)$ (Case 4, $L_z^+=7360$).

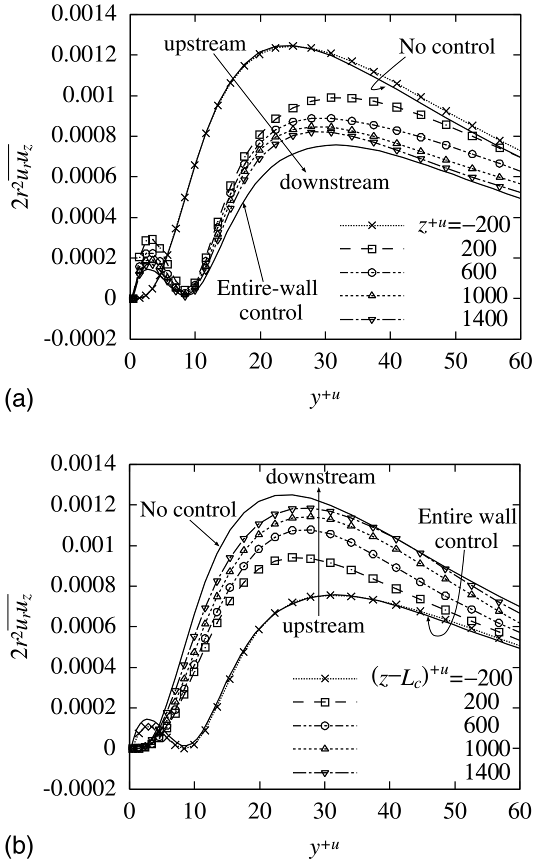

Fig. 9. Weighted Reynolds stress distribution at different streamwise locations (Case 4, $L_\mathrm{c}^{+\mathrm{u}}=7360$, $y_\mathrm{d}^{+\mathrm{u}}=15$): (a) controlled region; (b) uncontrolled region.

The radial distribution of the weighted Reynolds shear stress, $2r^2\overline{u_r'u_z'}$, at different streamwise locations are depicted in Fig. 9. Before entering into the controlled region ($z^{+\mathrm{u}}=-200$ in Fig. 9a), the profile is essentially the same as that of the uncontrolled flow. At the beginning of controlled region ($z^{+\mathrm{u}}=200$), the profile near the wall, say $y^{+\mathrm{u}}<40$, drastically changes to one similar to that of the entire-wall control. Detailed inspection reveals that the most of such streamwise evolution occurs in the region of $-10<z^{+\mathrm{u}}<50$. The far-wall distribution gradually changes following the quick change in the near-wall region. A similar variation is observed also in the uncontrolled region (Fig. 9b). Most of the change in the near-wall region occurs right downstream of the controlled region. After that, the profile recovers to that of the uncontrolled flow.

The causes for the variation of the weighted Reynolds stress in Fig. 9 can be investigated by examining its budget. An ordinary budget equation of the Reynolds shear stress is given as (see, e.g., Moser and Moin, 1984)

$$0=P_{rz}-\varepsilon_{rz}+\phi_{rz}+D_{rz}+C_{rz}^{(r)}+C_{rz}^{(z)}, \tag{8}$$

where P_{rz}, ε_{rz}, ϕ_{rz}, D_{rz}, $C_{rz}^{(r)}$ and $C_{rz}^{(z)}$ are the production, the dissipation, the pressure–strain, the diffusion (i.e., summation of all diffusion terms), and the radial and the streamwise mean convection terms, respectively, i.e.,

$$P_{rz}=-\overline{u_r'u_r'}\,\overline{u}_{z,r}-\overline{u_z'u_z'}\,\overline{u}_{r,z}, \tag{9}$$

$$\varepsilon_{rz}=2Re^{-1}[\overline{u'_{r,r}u'_{z,r}}+r^{-2}\overline{(u'_{r,\theta}-u'_\theta)(u'_{z,\theta})}+\overline{u'_{r,z}u'_{z,z}}], \tag{10}$$

$$\phi_{rz}=\overline{p'(u'_{r,z}+u'_{z,r})}, \tag{11}$$

$$D_{rz} = \underbrace{-\frac{1}{r}(r\overline{u'_r u'_r u'_z})_{,r} - (\overline{u'_r u'_z u'_z})_{,z} + r^{-1}\overline{u'_\theta u'_\theta u'_z}}_{\text{turbulent}}$$
$$\underbrace{-r^{-1}(\overline{rp'u'_z})_{,r} - (\overline{p'u'_r})_{,z} + r^{-1}\overline{u'_z p'}}_{\text{pressure}}$$
$$\underbrace{+Re^{-1}[r^{-1}\{r(\overline{u'_r u'_z})_{,r}\}_{,r} + (\overline{u'_r u'_z})_{,zz} - r^{-2}\overline{u'_r u'_z}]}_{\text{viscous}}, \tag{12}$$

$$C^{(r)}_{rz} = -\overline{u_r}(\overline{u'_r u'_z})_{,r}, \tag{13}$$

$$C^{(z)}_{rz} = -\overline{u_z}(\overline{u'_r u'_z})_{,z}. \tag{14}$$

Here, the subscripts with a comma ($,r$ and $,z$) denote spatial derivatives. Note that among the right-hand side terms in Eq. (12), the third, sixth and ninth terms are not actually diffusive. These terms express superficial redistribution due to the curvature of the coordinates. However, here we follow the convention to include them in the diffusion term.

Since the streamwise variation of the weighted Reynolds stress is of interest here, we rearrange Eq. (8) in a form:

$$\frac{\partial(2r^2\overline{u'_r u'_z})}{\partial z} = \widehat{P_{rz}} - \widehat{\varepsilon_{rz}} + \widehat{\phi_{rz}} + \widehat{D_{rz}} + \widehat{C^{(r)}_{rz}}, \tag{15}$$

where the hat represents the weighting operator defined as

$$\widehat{f} = \frac{2r^2}{\overline{u_z}} f. \tag{16}$$

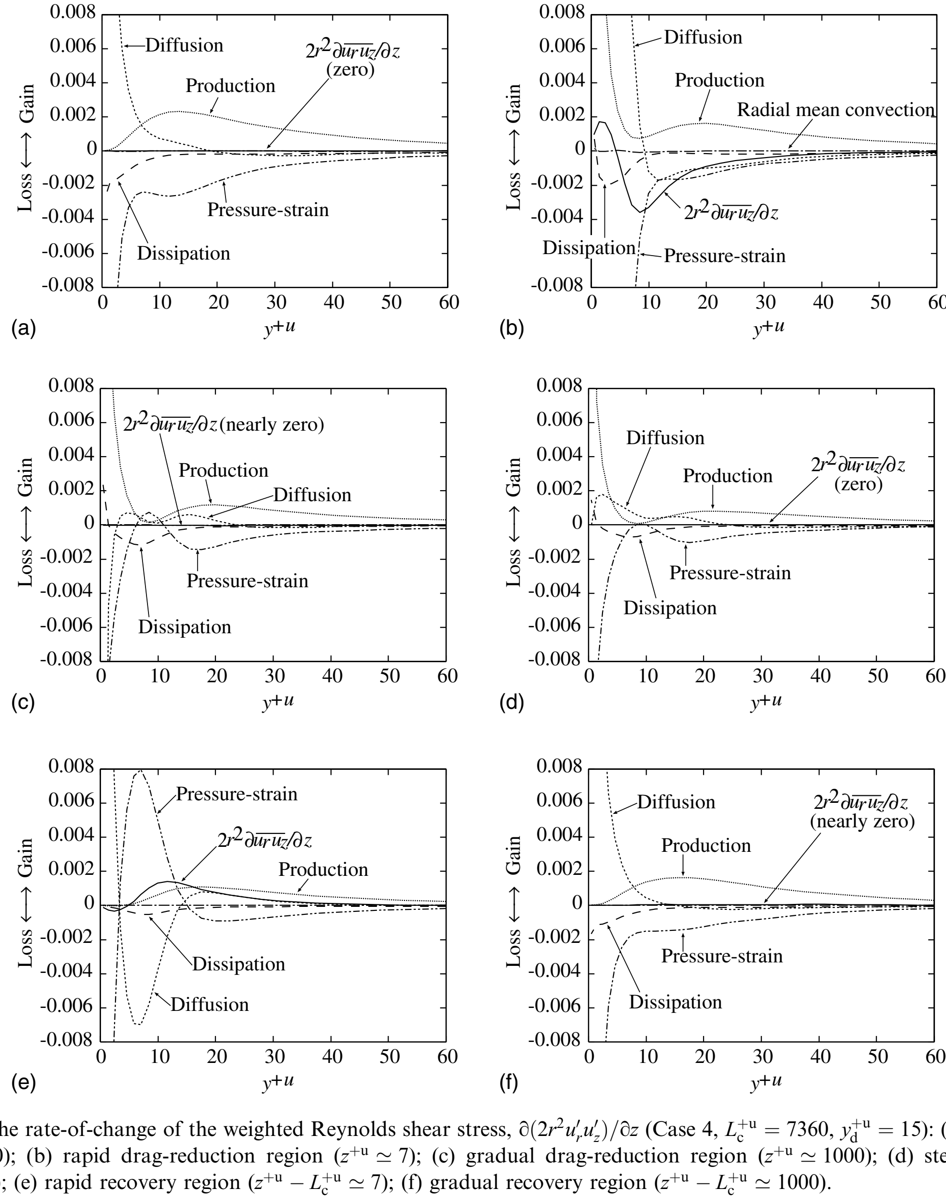

Fig. 10. Budget on the rate-of-change of the weighted Reynolds shear stress, $\partial(2r^2u'_r u'_z)/\partial z$ (Case 4, $L_c^{+u} = 7360$, $y_d^{+u} = 15$): (a) steady uncontrolled region ($z^{+u} \simeq -1000$); (b) rapid drag-reduction region ($z^{+u} \simeq 7$); (c) gradual drag-reduction region ($z^{+u} \simeq 1000$); (d) steady controlled region ($z^{+u} - L_c^{+u} \simeq -1000$); (e) rapid recovery region ($z^{+u} - L_c^{+u} \simeq 7$); (f) gradual recovery region ($z^{+u} - L_c^{+u} \simeq 1000$).

The left-hand side of Eq. (15) represents the streamwise rate-of-change of the weighted Reynolds stress. The right-hand side terms are the contributions from different dynamical components which have the same meanings as those in Eq. (8).

The balance based on Eq. (15) at various streamwise locations is shown in Fig. 10. In the steady uncontrolled region (Fig. 10a), the production-oriented term (hereafter called simply as the production term and the same for the other terms) and the pressure–strain term balance each other in the far-wall region. Near the wall, the pressure–strain term is balanced by the diffusion term. This trend of balance is the same as that of the ordinary budget of the Reynolds shear stress in the uncontrolled channel (Mansour et al., 1988) and pipe flows (Eggels et al., 1994). In the rapid drag reduction region (Fig. 10b), the profiles drastically change near the wall, whilst they remain essentially the same in the far-wall region. Especially, the pressure–strain term largely drops around $y^{+\mathrm{u}} \simeq 9$. Although most of this change is canceled by the diffusion (to be specific, the pressure diffusion) term, the difference, i.e., a strongly negative velocity–pressure gradient correlation, results in the large negative values of $\partial(2r^2\overline{u'_r u'_z})/\partial z$. It should be recalled that the area enclosed by the curve of $\partial(2r^2\overline{u'_r u'_z})/\partial z$ and the zero axis is nearly proportional to $\partial C_\mathrm{f}/\partial z$. Therefore, one can conclude that the rapid reduction of the drag in this region is caused by rapid drop of the velocity–pressure gradient correlation.

In the gradual reduction region (Fig. 10c) and in the steady controlled region (Fig. 10d) the trends are essentially the same. Around the virtual wall, all the terms are nearly zero. Above the virtual wall, the production term is balanced by the pressure–strain term. Below the virtual wall, the balance holds among the production, the diffusion and the pressure–strain terms. Similarly to Fig. 10a, all the terms are balanced somehow across the cross section, and therefore $\partial(2r^2\overline{u'_r u'_z})/\partial z$ is very small (Fig. 10c) or zero (Fig. 10d).

In the rapid recovery region (Fig. 10e), the profiles remain the same in the far-wall region and drastic change occurs near the wall. This is quite similar to the change observed in the transition from Fig. 10a to 10b. Around the location where the virtual wall has existed, a strong positive pressure–strain correlation is formed. Again, the most of this is canceled by the pressure diffusion, but the difference between them (i.e., a positive velocity–pressure gradient correlation) results in a large rate-of-change of the weighted Reynolds stress. Finally, in the gradual recovery region (Fig. 10f), the balance is essentially the same as that of the steady uncontrolled region (Fig. 10a) and therefore $\partial(2r^2\overline{u'_r u'_z})/\partial z$ is very small.

4.3. Velocity–pressure gradient correlation

As discussed above, the rapid recovery occurring right downstream of the controlled region is a consequence of the generation of Reynolds shear stress due to a positive velocity–pressure gradient correlation, i.e.,

$$\Pi_{rz} = -\overline{u'_z p'_{,r}} - \overline{u'_r p'_{,z}} > 0, \qquad (17)$$

which is not usually observed in uncontrolled flows (see, e.g., Mansour et al., 1988; Eggels et al., 1994). The present statistics show that the second term of Eq. (17) is much smaller than the first term, and therefore the positive value of Π_{rz} is due to correlation between the streamwise velocity fluctuation, u'_z, and the fluctuating radial pressure gradient, $p'_{,r}$.

The cause for this characteristic velocity–pressure gradient correlation is investigated by visualization of the flow around the interface of controlled and uncontrolled regions. Fig. 11a visualizes a region where the control ends with blowing. In the controlled region, i.e., $(z - L_\mathrm{c})^{+\mathrm{u}} < 0$, a virtual wall can clearly be observed around $y^{+\mathrm{u}} \simeq 9$. This implies that the sweeping motion from toward the wall is balanced by the blowing. Around $z = L_\mathrm{c}$, a locally low pressure region appears. This is because the blowing from the wall, that is expected to further exist, suddenly stops. The sweeping motion is thus no longer pressed back by the opposing

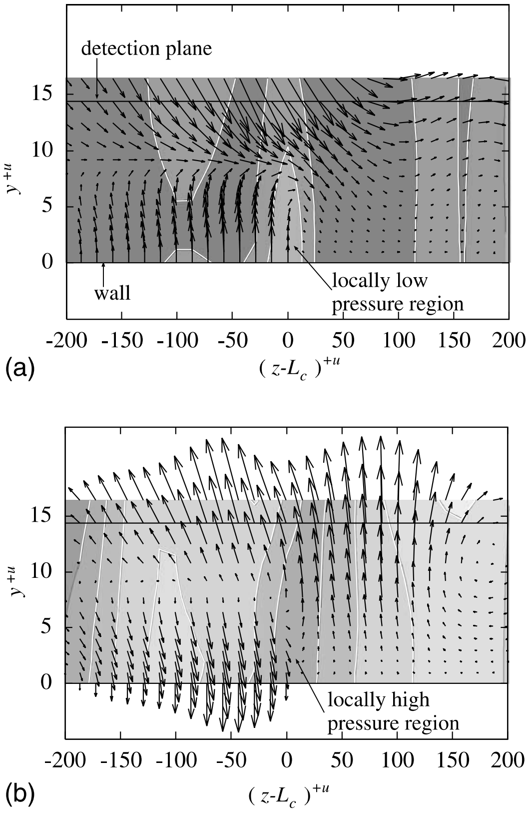

Fig. 11. Fluctuating velocity vector ($\vec{u}'$) and pressure (light gray, $(p')^{+\mathrm{u}} < -1.5$, to dark gray $(p')^{+\mathrm{u}} > 1.5$ with increment of 0.5) around the end point of control projected to an r–z plane (Case 4, $L_\mathrm{c}^{+\mathrm{u}} = 7360$, $y_\mathrm{d}^{+\mathrm{u}} = 15$): (a) in a region where the control ends with blowing; (b) the same with suction. The coordinates and the vectors are stretched (10 times) in the wall-normal direction.

flow from the wall and it makes an inward rush. Fig. 11b, on the other hand, visualizes a region where the control ends with suction. A phenomenon nearly opposite to that in the blowing case can be seen. Namely, a relation, i.e.,

$$\left.\begin{array}{lll} u'_z > 0, & p'_{,r} < 0 & \text{(blowing case)} \\ u'_z < 0, & p'_{,r} > 0 & \text{(suction case)} \end{array}\right\} \Rightarrow -u'_z p'_{,r} > 0, \tag{18}$$

holds in both cases to result in a positive velocity–pressure gradient correlation in this region.

Fig. 12 shows the correlations between the blowing/suction velocity in the terminal control region and the quantities concerning the velocity–pressure correlation in the right downstream. In Fig. 12a, clear negative correlation with the upstream blowing/suction velocity can be found for the streamwise velocity fluctuation, u'_z. Namely, high-speed streaks frequently appear downstream when the control ends with blowing ($u_{r,\mathrm{wall}} < 0$) and low-speed streaks after suction ($u_{r,\mathrm{wall}} > 0$). The positive correlation for the radial pressure gradient (Fig. 12b) is much clearer. Fig. 12a and b support that the velocity and pressure fields shown in Fig. 11 are not special, but typical ones. The correlation between the upstream blowing/suction velocity and the first term in Eq. (17) right downstream is shown in Fig. 12c. There seems to exist a threshold at $|u_{r,\mathrm{wall}}| \simeq 0.005$ ($|u^{+\mathrm{u}}_{r,\mathrm{wall}}| \simeq 0.15$), above which $-u'_z p'_{,r}$ becomes mostly positive.

Table 2 quantitatively shows the contribution to Π_{rz} right downstream of the controlled region, conditioned by the upstream blowing/suction velocity. The strong blowing ($u_{r,\mathrm{wall}} < -0.005$) is the main contributor to the strongly positive value of Π_{rz} despite its low frequency. The strong suction ($u_{r,\mathrm{wall}} > 0.005$) is the next contributor. The weak blowing/suction ($|u_{r,\mathrm{wall}}| < 0.005$) frequently occurs, but its contribution to Π_{rz} is small. A similar analysis made by using blowing/suction velocity at different streamwise locations reveals that only the strong blowing/suction in the right upstream region, say $-200 < (z - L_\mathrm{c})^{+\mathrm{u}} < 0$, have such contribution to Π_{rz} downstream.

5. Modification of the partial-wall control

5.1. Attempt to avoid the rapid recovery right downstream of controlled region

Attempts are made to modify the control input so that higher average drag reduction rate can be attained even with finite a length of controlled region. Based on the information above, one may improve the control performance by avoiding the rapid recovery that occurs right downstream of the controlled region.

Here, three primitive modifications are considered:

- (Case A) Damping of the amplitude of control input in the terminal control region.
- (Case B) Similar damping to Case A, but only to the control input that exceeds the above-mentioned threshold, i.e., $|u_{r,\mathrm{wall}}| > 0.005$.
- (Case C) A conditional damping similar to Case B with a condition of $u_{r,\mathrm{wall}} < -0.005$ (i.e., strong blowing).

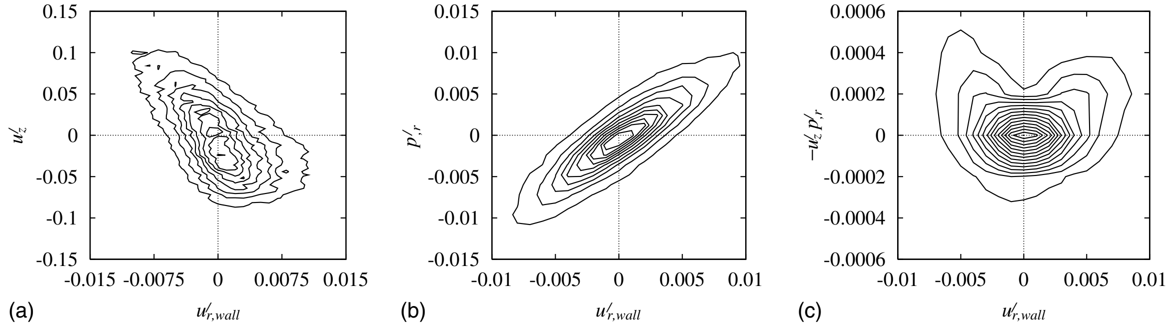

Fig. 12. Correlations between terminal control input, $u_{r,\mathrm{wall}}$ ($z^{+\mathrm{u}} \simeq L_\mathrm{c}^{+\mathrm{u}} - 7$) and quantities right downstream ($y^{+\mathrm{u}} \simeq 10, z^{+\mathrm{u}} \simeq L_\mathrm{c}^{+\mathrm{u}} + 7$), displayed as isocontours of the probability density function: (a) streamwise velocity fluctuation, u'_z; (b) fluctuating pressure gradient, $p'_{,r}$; (c) the first term in Eq. (17), i.e., $-u'_z p'_{,r}$.

Table 2
Contribution to the velocity–pressure gradient correlation right downstream of controlled region, conditioned by the upstream blowing/suction velocity (102,400 samples)

Terminal control input	$u_{r,\mathrm{wall}} < -0.005$ (strong blowing)	$\lvert u_{r,\mathrm{wall}}\rvert < 0.005$ (weak control)	$u_{r,\mathrm{wall}} > 0.005$ (strong suction)
Frequency of the event [%]	15.3	68.8	15.9
Contribution to Π_{rz} [%]	66.8	11.3	21.9

Especially, Cases B and C are motivated by the analysis in the previous section that the strong blowing/suction in the terminal control region is closely related to the positive velocity–pressure gradient correlation. In the present study, a linear damping is applied from $z = L_d$ located upstream of $z = L_c$. For Case A, the control input, Eq. (1), is simply modified to read,

$$u_r(R, \theta, z, t) = -\alpha(z) u_r(R - y_d, \theta, z, t), \tag{19}$$

where $\alpha = 1$ in $0 \leqslant z \leqslant L_d$ and $\alpha = (L_c - z)/(L_c - L_d)$ in $L_d \leqslant z \leqslant L_c$. For Cases B and C, Eq. (19) is applied only when $u_{r,\mathrm{wall}}$ meets the above-mentioned conditions. In these cases, zero net flux is ensured by subtracting the mean control velocity.

Fig. 13 shows the variation of the normalized skin friction around the terminal edge of the controlled region. The starting location of damping is set at $L_d^{+u} = L_c^{+u} - 184$, because the control input right upstream $(-200 < (z - L_c)^{+u} < 0)$ is most related to the positive velocity–pressure correlation downstream, as mentioned above. The other parameters are $L^{+u} = 7360$, $L_c^{+u} = 3680$ and $y_d^{+u} = 10$. In all the cases, the rapid recovery is slightly relaxed. However, the recovery begins earlier than the original case due to the damped control input, and it results in poorer global control effects.

5.2. Attempt to hinder the secondary gradual recovery

Another possibility to improve the control performance is to hinder the gradual recovery that follows the rapid recovery. As suggested from the analysis in the previous section, it requires a modification of the large-scale flow structure. One candidate to do this is a uniform blowing/suction. Only a small amount of uniform suction can largely reduce the Reynolds stress (Sumitani and Kasagi, 1995), although the total skin friction increases due to the positive mean convective contribution (Fukagata et al., 2002). Uniform blowing, on the other hand, enlarges the Reynolds stress, while the friction reduces due to the negative mean convective contribution.

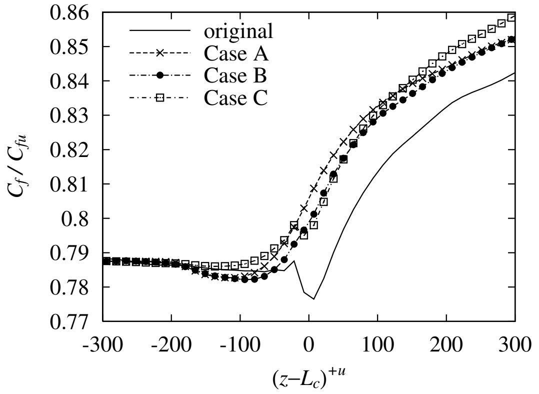

Fig. 13. Variation of normalized local skin friction around the interface between controlled and uncontrolled region (modified control to avoid the rapid recovery).

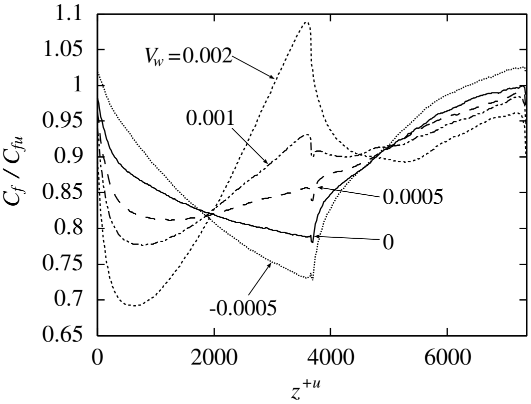

Fig. 14. Variation of normalized local skin friction (modified control to hinder the gradual recovery).

Here we consider a following modification to the control input:

$$u_r(R, \theta, z, t) = -u_r(R - y_d, \theta, z, t) + U_{r,\mathrm{wall}}(z), \tag{20}$$

where $U_{r,\mathrm{wall}}(z)$ is the blowing/suction which is a function only of z and uniform in θ direction, and is set as $U_{r,\mathrm{wall}}(z) = V_w(z - L_c/2)/L_c$. Namely, it linearly varies from $U_{r,\mathrm{wall}} = -V_w$ at $z = 0$ to $U_{r,\mathrm{wall}} = V_w$ at $z = L_c$. Basically, V_w is set positive so that the excessive Reynolds stress caused by the uniform blowing in the initial controlled region can be reduced by the opposition control, whilst the at the terminal edge the Reynolds stress can largely be suppressed due to the uniform suction.

Fig. 14 shows the result. Drastic change is observed in the profiles as V_w varies. Especially, with $V_w = 0.002$, which is comparable to the value used by Sumitani and Kasagi (1995), the gradual recovery is much hindered. Unlike the initial expectation, however, the average drag reduction rate is unchanged. The main reason for this failure is that the skin friction coefficient around the terminal control region is almost exclusively determined by the mean convective contribution due to the uniform suction (Fukagata et al., 2002).

6. Conclusions

The opposition control was applied to DNS of turbulent pipe flow. From the simulation with control on the entire surface, we found that the maximum drag reduction rate is comparable to that of channel flow (∼25%) despite that the surface area per volume of a pipe is twice as large as that of a channel.

From the simulation with the control on partial surface, the following results were obtained:

(1) Even if the control is not applied on an entire surface, the average drag reduction proportional to the area of control can be obtained.
(2) The local skin friction coefficient exhibits a complex streamwise variation despite the simple relation for the average drag reduction rate.
(3) The flow recovers to the uncontrolled state about $11R$–$14R$ downstream of the controlled region.
(4) The rapid recovery of the skin friction is observed right downstream of the controlled region.

The complex variation of the skin friction coefficient is essentially due to the variation of the radial Reynolds stress distribution. That variation can be divided into two phenomena with different length scales: one is short $\ell_z^{+u} \sim 10$ and limited near the wall ($y^{+u} < 40$), the other is long ($\ell_z \sim R$) and covers entire height from the wall to the pipe axis. The short-scale phenomenon is responsible for the initial rapid recovery, whereas the long-scale one is for the subsequent gradual recovery. The cause of the rapid recovery is a positive velocity–pressure gradient correlation created by the interaction between the strong blowing right upstream of the terminal edge of the controlled region and the following inward rush due to the collapse of the virtual wall.

Based on the knowledge acquired, some attempts were made to modify the control input for a better control performance. The rapid recovery can be relaxed to some extent by damping the terminal control input. The subsequent large-scale gradual recovery can be hindered by superimposing a uniform blowing/suction to the control input. Unfortunately, however, the overall control performance could not be improved by these modifications.

Our final goal is to determine the optimal control input when a control unit of a finite length is given. Although further extensive investigation is required, we believe that the present study revealed some fundamental phenomena in such system and provided some clues towards that goal.

Acknowledgements

This work was supported through the Project for Organized Research Combination System by the Ministry of Education, Culture, Sports and Technology of Japan (MEXT).

References

Chang, Y., Collis, S.S., Ramakrishnan, S., 2002. Viscous effects in control of near-wall turbulence. Phys. Fluids 14 (11), 4069–4080.

Choi, H., Moin, P., Kim, J., 1994. Active turbulence control for drag reduction in wall bounded flows. J. Fluid Mech. 262, 75–110.

Eggels, J.G.M., Unger, F., Weiss, M.H., Westerweel, J., Adrian, R.J., Friedrich, R., Nieuwstadt, F.T.M., 1994. Fully developed turbulent pipe flow: a comparison between direct numerical simulation and experiment. J. Fluid Mech. 268, 175–209.

Endo, T., Kasagi, N., Suzuki, Y., 2000. Feedback control of wall turbulence with wall deformation. Int. J. Heat Fluid Flow 21 (5), 568–575.

Fukagata, K., Kasagi, N., 2002. Highly energy-conservative finite difference method for the cylindrical coordinate system. J. Comp. Phys. 181 (2), 478–498.

Fukagata, K., Iwamoto, K., Kasagi, N., 2002. Contribution of Reynolds stress distribution to the skin friction in wall-bounded flows. Phys. Fluids 14 (11), L73–L76.

Hammond, E.P., Bewley, T.R., Moin, P., 1998. Observed mechanisms for turbulence attenuation and enhancement in opposition-controlled wall-bounded flows. Phys. Fluids 10 (9), 2421–2423.

Iwamoto, K., Suzuki, Y., Kasagi, N., 2002. Reynolds number effect on wall turbulence: toward effective feedback control. Int. J. Heat Fluid Flow 23 (5), 678–689.

Le, H., Moin, P., Kim, J., 1997. Direct numerical simulation of turbulent flow over a backward-facing step. J. Fluid Mech. 330, 349–374.

Lee, C., Kim, J., Choi, H., 1998. Suboptimal control of turbulent channel flow for drag reduction. J. Fluid Mech. 358, 245–258.

Mansour, N.N., Kim, J., Moin, P., 1988. Reynolds-stress and dissipation-rate budgets in a turbulent channel flow. J. Fluid Mech. 194, 15–44.

Moser, R.D., Moin, P., 1984. Direct numerical simulation of curved turbulent channel flow. Report No. TF-20, Stanford University, pp. 83–87.

Rai, M.M., Moin, P., 1991. Direct numerical simulations of turbulent flow using finite difference schemes. J. Comp. Phys. 96 (1), 15–53.

Spalart, P.R., Moser, R.D., Rogers, M.M., 1991. Spectral methods for the Navier–Stokes equations with one infinite and two periodic directions. J. Comp. Phys. 96 (2), 297–324.

Sumitani, Y., Kasagi, N., 1995. Direct numerical simulation of turbulent transport with uniform wall injection and suction. AIAA J. 33 (7), 1220–1228.

Rathnasingham, R., Breuer, K.S. Closed loop control of turbulent boundary layers. J. Fluid Mech., submitted for publication.

Xu, C.-X., Choi, J.-I., Sung, H.J., 2002. Suboptimal control for drag reduction in turbulent pipe flow. Fluid Dyn. Res. 30 (4), 217–231.

Yoshino, T., Suzuki, Y., Kasagi, N., 2002. Development of genetic algorithm based feedback control system of wall turbulence. In: Proc. 5th JSME-KSME Fluids Engineering Conference, 17–21 November 2002, Nagoya, Japan (CD-ROM), Paper No. OS4-1, 5 p.